ACS Catalysis

Research Article

pubs.acs.org/acscatalysis

Microkinetic Simulation of Ammonia Oxidation on the $RuO_2(110)$ Surface

Chia-Ching Wang, Jyun-Yi Wu, Thong L. M. Pham, and Jyh-Chiang Jiang*

Department of Chemical Engineering, National Taiwan University of Science and Technology, 43, Keelung Road, Section 4, Taipei 106, Taiwan

Supporting Information

ABSTRACT: The investigation by microkinetic simulations provide detailed reaction mechanisms about the NH_3 oxidation on the $RuO_2(110)$ surface. There are 41 elementary reactions involved in the microkinetic model in which all the thermodynamic and kinetic parameters are obtained from density functional theory (DFT) calculations, and the entropy effects of each reaction are considered in the simulation. The differences in reaction mechanisms between the batch type and the steady state were characterized in this study. The selectivities to the oxidation products, including N_2, NO, and N_2O, depend on the oxidation conditions. The simulated results show that the O_2/NH_3 ratio, system temperature, and pressure are the controlling factors that could alter the results of the oxidation. The microkinetic modeling demonstrates how these parameters affect the NH_3 conversion and the selectivities. The simulations showed that N_2 and NO could be a primary product under different oxidizing conditions; however, N_2O could only be a minor product because of the nature of its formation mechanism. The highest N_2O selectivity obtained in the simulations is 30%.

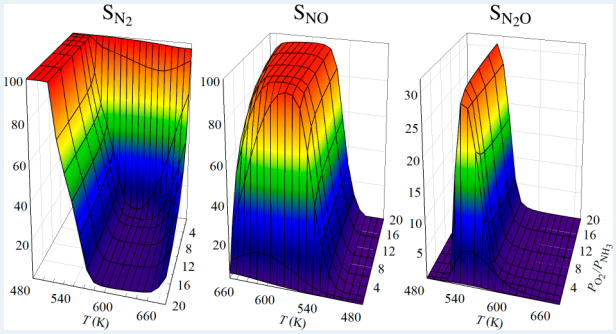

KEYWORDS: *ruthenium dioxide, NH_3, catalyst, DFT, microkinetics, selectivity, N_2O*

1. INTRODUCTION

Microkinetic modeling is a convenient tool for consolidation of vital information about a catalytic process, such as the reaction orders, reversible or irreversible nature, selectivity, and turnover frequency (TOF). To construct a microkinetic model, researchers need to establish sequences of elementary reactions, such as adsorption, desorption, and surface reaction, and then derive the parameters inside. Unfortunately, it is difficult to extract all kinetic and thermodynamic parameters in all elementary reactions from experimental data. Therefore, it is vital to employ theoretical approaches such as density functional theory (DFT) calculations to estimate the parameters required for the microkinetic modeling and reduce the need to simplify assumptions in microkinetic models. In recent years, there has been remarkable progress in the implementation of DFT methods in the development of microkinetic models in heterogeneous catalysis.[1−10] Because of the developments in quantum mechanics and remarkable advances of computing capability, ab initio methods can now be used for rigorous determinations of the parameters in heterogeneous catalytic reactions, such as enthalpies, entropies, reaction barriers, and frequency factors. In addition, the active intermediates and inactive spectator species in the reactions can be characterized by using these techniques.

Recently, we successfully simulated temperature-programmed desorption (TPD) spectra of the $RuO_2(110)$ surface by applying microkinetic modeling.[11] The $RuO_2(110)$ surface has high catalytic ability for oxidation reactions of NH_3,[12−16] HCl,[17,18] and CO.[19,20] In 2005, the experiments by Wang et al. showed that a single crystal $RuO_2(110)$ surface exhibits high catalytic activity for NH_3 oxidation under ultrahigh vacuum (UHV).[12] The authors found that the system reaches ∼100% NO selectivity when O_2/NH_3 = 20 at 530 K. However, the ambient-pressure experiments by Pérez-Ramírez et al. showed that the NO selectivity does not exceed 65% at O_2/NH_3 = 140 over polycrystalline RuO_2.[15] In addition, Cui et al. reported 80% of N_2 selectivity in NH_3 oxidation over mesoporous RuO_2 when O_2/NH_3 = 20.[16]

Another remarkable difference between the oxidation conditions is the production of N_2O. Wang et al. demonstrated the absence of N_2O in oxidation products,[12] but Pérez-Ramírez et al. reported a 25% N_2O selectivity in the ammonia oxidation.[15] The mismatch in the distribution of products between these studies can be related to pressure or materials gaps, and a further investigation about the reaction mechanisms is required. In 2010, Hong et al. simulated ammonia oxidation on the $RuO_2(110)$ surface by combining DFT calculations and the kinetic Monte Carlo (KMC) method.[14] The authors showed the importance of N and O diffusion on the surface and how they affect the selectivities in the oxidations. However, they considered only 18 elementary reactions in their KMC

Received: July 11, 2013
Published: January 8, 2014

   dx.doi.org/10.1021/cs401070n | ACS Catal. 2014, 4, 639−648

model, and the reactions related to the N_2O molecule were not involved. Moreover, the authors did not consider the entropy effects and applied 10^{13} s^{-1}, a generally applied empirical value, as the pre-exponential factor. Nevertheless, the pre-exponential factor should be a temperature-dependent parameter, and it will be much larger than 10^{13} s^{-1} in desorption processes.[9,11]

In this work, we establish a new microkinetic model to simulate ammonia oxidation reactions. To investigate a more detailed ammonia oxidation mechanism on the $RuO_2(110)$ surface, 41 elementary reactions including entropy effects are adopted in our microkinetic model. We characterize the effects from temperature, O_2 and NH_3 pressure ratios (P_{O_2}/P_{NH_3}), and system total pressure and analyzed how they influence the selectivity and NH_3 conversion in ammonia oxidation.

2. METHODS

In a heterogeneous catalytic system, the elementary reactions include adsorption, desorption, and surface reactions. In microkinetic modeling, the rates of the adsorption (r_{ads}) and desorption (r_{des}) of species A can be defined as

$$r_{ads}(t) = k_{ads} Y_A \theta_* \tag{2-1}$$

$$r_{des}(t) = k_{des} \theta_{A*} \tag{2-2}$$

where $k(s^{-1})$ is the rate constant, and the dimensionless Y_A, θ_*, and θ_{A*} are the mole fraction of A in gas phase, coverage of the free site, and coverage of the adsorbed molecule on the surface, respectively. In our previous study,[11] we derived the rate constants of adsorption (k_{ads}) and desorption (k_{des}) from the collision theory. They are

$$k_{ads} = \frac{P_T}{C_T\sqrt{2\pi m_A k_B T}} \tag{2-3}$$

$$k_{des} = \frac{P_T}{C_T\sqrt{2\pi m_A k_B T}} \frac{q_A q_*}{q_{A*}} e^{-E_{des}/RT} \tag{2-4}$$

and the pre-exponential factor of the desorption process (ν_{des}) is

$$\nu_{des} = \frac{P_T}{C_T\sqrt{2\pi m_A k_B T}} \frac{q_A q_*}{q_{A*}} \tag{2-5}$$

In eq 2-3−2-5, P_T is the total pressure of the system; C_T (m^{-2}) is the Ru_{cus} (cus = coordinatively unsaturated site) concentration of reaction sites per unit area on the surface ($C_T = 5.05 \times 10^{18}$ m^{-2} in this work); m_A is the molecular weight of species A; k_B is the Boltzmann constant; and q is the partition functions of molecular A (q_A), clean surface (q_*), and adsorbed A (q_{A*}). The terms of the partition function are summarized in the Supporting Information. For surface reactions, the rate constant (k_{sr}) is defined by transition state theory,

$$k_{sr} = \frac{k_B T}{h} \frac{q_{TS}}{q_{IS}} e^{-E^{\ddagger}/RT} \tag{2-6}$$

where h is the Plank's constant, $E^{\ddagger}$ is the energy barrier, and q_{IS} and q_{TS} are the partition functions of the initial and transition states.

$$E_a = E^{\ddagger} + RT \tag{2-7}$$

where E_a is the activation energy. By introducing eq 2-7 into eq 2-6, the rate constant of surface reactions becomes

$$k_{sr} = e\frac{k_B T}{h} \frac{q_{TS}}{q_{IS}} e^{-E_a/RT} \tag{2-8}$$

and the pre-exponential factor of surface reactions (ν_{sr}) is

$$\nu_{sr} = e\frac{k_B T}{h} \frac{q_{TS}}{q_{IS}} \tag{2-9}$$

Because the rate equations of all the elementary reactions are defined, the following step in the microkinetic modeling is set up as ordinary differential equations (ODEs). On the basis of the mass balance, each ODE describes the relationship between the coverage (θ) and time (t) of each surface species in the microkinetic model. Then the fractional coverages of the surface species as a function of time can be evaluated by solving a system of ODEs. Here, all the ODEs were solved by the numerical method using *Mathematica*. In this study, we simulated two oxidation methods: the batch type oxidation and the steady-state oxidation. For the batch type oxidation, the NH_3 and O_2 molecules are preadsorbed onto the $RuO_2(110)$ surface at 90 K, and oxidation proceeds when the surface is heated up. For steady-state oxidation, the reaction proceeds under a constant system temperature and a fixed partial pressure of NH_3 and O_2.

All the thermodynamic and kinetic parameters of each elementary reaction were obtained by DFT calculations. The DFT calculations were performed using the Vienna Ab Initio Simulation Package (VASP).[21−23] The generalized gradient approximation (GGA) was used with the functional described by Perdew and Wang,[24] and a cutoff energy of 450 eV was applied for all calculations. Electron−ion interactions were investigated using the projector augmented wave method;[25] spin-polarized calculations were performed for all of the structural optimizations. The nudged elastic band method was applied to locate the transition states (TSs). The validity of all the optimized structures and the determined TSs were checked through normal-mode frequency analysis. For a real minimum on a potential energy surface, all frequencies must be positive; a TS must have one imaginary frequency corresponding to the reaction coordinate. The $RuO_2(110)$ surface was modeled as a two-dimensional slab in a three-dimensional periodic cell. The slab was a 3 × 1 surface having the thickness of three O−Ru−O repeat units, which is equivalent to 9 atomic layers. A 13 Å vacuum space was introduced in the [110] direction to curtail interactions between the slabs. The upper four atomic layers were relaxed in all structural optimizations. In the vibrational frequency calculations, only the upper two atomic layers and adsorbates were relaxed. For this (3 × 1)-$RuO_2(110)$ surface model, the k-points of 4 × 6 × 1 were set by Monkhorst−Pack.

The desorption energies of the reactants and products were calculated using the formula

$$E_{des} = (E_{RuO_2} + E_A) - E_{A/RuO_2} \tag{2-10}$$

and the adsorption energies are defined by

$$E_{ads} = -E_{des} \tag{2-11}$$

In eq 2-10, E_A is the energy of a single adsorbate in the gas phase, E_{RuO_2} is the energy of the clean surface, and E_{A/RuO_2} is the total energy of the adsorption system. A positive value of E_{des} indicates an endothermic desorption process. In this work, all the energies introduced into the rate equations were corrected by the zero-point energy (ZPE).

dx.doi.org/10.1021/cs401070n | ACS Catal. 2014, 4, 639−648

Table 1. Elementary Reactions in Ammonia Oxidation on the $RuO_2(110)$ Surface and the Corresponding ZPE Corrected Energetics ($E^{\ddagger}$ and ΔE in eV) and Kinetic (ν and k in s^{-1}) Parameters[a]

				ν		k	
no.	reaction	$E^{\ddagger}$	ΔE[b]	90 K	670 K	90 K	670 K
Adsorption−Desorption							
R1	$NH_{3(g)} + Ru_{cus} \rightarrow NH_{3\text{-}cus}$		−1.36 (−1.51)			2.67×10^{-6}	9.77×10^{-7}
R2	$NH_{3\text{-}cus} \rightarrow NH_{3(g)} + Ru_{cus}$		1.36 (1.51)	1.43×10^{15}	1.70×10^{16}	2.23×10^{-53}	1.33×10^{7}
R3	$O_{2(g)} + 2Ru_{cus} \rightarrow O_{2\text{-}cus}$		−1.21 (−1.26)			1.94×10^{-6}	7.13×10^{-7}
R4	$O_{2\text{-}cus} \rightarrow O_{2(g)} + 2Ru_{cus}$		1.21 (1.26)	5.07×10^{15}	1.96×10^{16}	7.90×10^{-53}	1.52×10^{7}
R5	$N_{2\text{-}cus} \rightarrow N_{2(g)} + Ru_{cus}$		0.59 (0.65)	2.61×10^{15}	5.42×10^{15}	1.53×10^{-18}	1.86×10^{11}
R6	$NO_{cus} \rightarrow NO_{(g)} + Ru_{cus}$		2.00 (2.12)	4.01×10^{15}	1.83×10^{16}	4.50×10^{-97}	1.67×10^{1}
R7	$N_2O_{cus} \rightarrow N_2O_{(g)} + Ru_{cus}$		0.51 (0.56)	3.78×10^{16}	5.29×10^{16}	8.56×10^{-13}	7.51×10^{12}
R8	$H_2O_{cus} \rightarrow H_2O_{(g)} + Ru_{cus}$		1.00 (1.14)	1.30×10^{15}	1.28×10^{17}	1.90×10^{-41}	4.04×10^{9}
R9	$H_2O_{br} \rightarrow H_2O_{(g)} + Ru_{br}$		0.84 (0.95)	3.51×10^{15}	2.34×10^{24}	2.12×10^{-32}	1.06×10^{18}
NH_x (x = 1−3) Dehydrogenations							
R10	$NH_{3\text{-}cus} + O_{br} \rightarrow NH_{2\text{-}cus} + OH_{br}$	0.35 (0.46)	0.38 (0.44)	3.93×10^{12}	3.50×10^{12}	4.75×10^{-10}	1.67×10^{12}
R11	$NH_{2\text{-}cus} + OH_{br} \rightarrow NH_{3\text{-}cus} + O_{br}$	0.00 (0.02)	−0.38 (−0.44)	4.55×10^{12}	6.06×10^{12}	1.67×10^{12}	2.23×10^{12}
R12	$NH_{3\text{-}cus} + O_{cus} \rightarrow NH_{2\text{-}cus} + OH_{cus}$	0.46 (0.59)	0.50 (0.57)	4.53×10^{12}	9.60×10^{12}	1.56×10^{-16}	6.07×10^{8}
R13	$NH_{2\text{-}cus} + OH_{cus} \rightarrow NH_{3\text{-}cus} + O_{cus}$	0.00 (0.02)	−0.50 (−0.57)	7.22×10^{12}	2.68×10^{13}	2.66×10^{12}	9.86×10^{12}
R14	$NH_{2\text{-}cus} + O_{br} \rightarrow NH_{cus} + OH_{br}$	0.63 (0.77)	0.58 (0.62)	5.35×10^{12}	1.22×10^{13}	9.80×10^{-24}	8.16×10^{7}
R15	$NH_{cus} + OH_{br} \rightarrow NH_{2\text{-}cus} + O_{br}$	0.05 (0.15)	−0.58 (−0.62)	3.77×10^{12}	5.72×10^{12}	2.21×10^{9}	8.85×10^{11}
R16	$NH_{2\text{-}cus} + O_{cus} \rightarrow NH_{cus} + OH_{cus}$	0.44 (0.54)	0.41 (0.47)	3.75×10^{12}	2.79×10^{12}	1.75×10^{-13}	4.65×10^{8}
R17	$NH_{cus} + OH_{cus} \rightarrow NH_{2\text{-}cus} + O_{cus}$	0.03 (0.07)	−0.41 (−0.47)	2.81×10^{12}	1.59×10^{12}	1.14×10^{10}	3.19×10^{11}
R18	$NH_{2\text{-}cus} + OH_{cus} \rightarrow NH_{cus} + H_2O_{cus}$	0.33 (0.46)	0.38 (0.40)	4.47×10^{12}	7.84×10^{12}	9.04×10^{-10}	4.02×10^{9}
R19	$NH_{cus} + H_2O_{cus} \rightarrow NH_{2\text{-}cus} + OH_{cus}$	0.00 (0.06)	−0.38 (−0.40)	4.98×10^{12}	2.27×10^{13}	1.83×10^{12}	8.34×10^{12}
R20	$NH_{cus} + O_{br} \rightarrow N_{cus} + OH_{br}$	0.04 (0.07)	−0.69 (−0.77)	4.79×10^{12}	1.78×10^{13}	1.71×10^{10}	3.50×10^{12}
R21	$N_{cus} + OH_{br} \rightarrow NH_{cus} + O_{br}$	0.73 (0.84)	0.69 (0.77)	6.17×10^{12}	6.81×10^{13}	4.23×10^{-29}	8.46×10^{7}
R22	$NH_{cus} + O_{cus} \rightarrow N_{cus} + OH_{cus}$	0.00 (0.00)		5.10×10^{12}	3.79×10^{13}	1.87×10^{12}	1.40×10^{13}
R23	$NH_{cus} + OH_{br} \rightarrow N_{cus} + H_2O_{br}$	0.43 (0.52)	0.32 (0.26)	5.55×10^{12}	1.96×10^{13}	9.40×10^{-13}	3.88×10^{9}
R24	$N_{cus} + H_2O_{br} \rightarrow NH_{cus} + OH_{br}$	0.11 (0.26)	−0.32 (−0.26)	5.72×10^{12}	2.70×10^{13}	1.00×10^{6}	1.41×10^{12}
R25	$NH_{cus} + OH_{cus} \rightarrow N_{cus} + H_2O_{cus}$	0.00 (0.00)		5.10×10^{12}	3.79×10^{13}	1.87×10^{12}	1.40×10^{13}
Oxidation Product Formations							
R26	$N_{cus} + N_{cus} \rightarrow N_{2\text{-}cus} + Ru_{cus}$	0.38 (0.46)	−3.85 (−3.88)	4.32×10^{12}	1.15×10^{13}	1.21×10^{-68}	7.31×10^{1}
R27	$N_{2\text{-}cus} + Ru_{cus} \rightarrow N_{cus} + N_{cus}$	4.23 (4.34)	3.85 (3.88)	4.64×10^{12}	1.11×10^{13}	4.29×10^{-225}	6.72×10^{-20}
R28	$N_{cus} + O_{cus} \rightarrow NO_{cus} + Ru_{cus}$	0.46 (0.48)	−1.86 (−1.92)	3.45×10^{12}	5.51×10^{12}	1.77×10^{-55}	2.12×10^{3}
R29	$NO_{cus} + Ru_{cus} \rightarrow N_{cus} + O_{cus}$	2.32 (2.40)	1.86 (1.92)	3.22×10^{12}	7.44×10^{12}	1.28×10^{-118}	9.53×10^{-6}
R30	$N_{cus} + NO_{cus} \rightarrow N_2O_{cus} + Ru_{cus}$	0.93 (1.00)	−0.85 (−0.87)	4.32×10^{12}	1.15×10^{12}	1.21×10^{-68}	7.31×10^{1}
R31	$N_2O_{cus} + Ru_{cus} \rightarrow N_{cus} + NO_{cus}$	1.78 (1.87)	0.85 (0.87)	5.20×10^{12}	2.16×10^{13}	6.42×10^{-88}	3.45×10^{-1}
R32	$OH_{cus} + OH_{cus} \rightarrow H_2O_{cus} + O_{cus}$	0.09 (0.20)	0.08 (0.05)	6.38×10^{12}	2.36×10^{13}	1.47×10^{7}	1.73×10^{12}
R33	$H_2O_{cus} + O_{cus} \rightarrow OH_{cus} + OH_{cus}$	0.01 (0.15)	−0.08 (−0.05)	5.42×10^{12}	2.38×10^{13}	1.96×10^{11}	6.42×10^{12}
R34	$OH_{cus} + OH_{br} \rightarrow H_2O_{cus} + O_{br}$	0.03 (0.17)	0.09 (0.09)	1.08×10^{13}	1.50×10^{14}	2.49×10^{7}	1.10×10^{13}
R35	$H_2O_{cus} + O_{br} \rightarrow OH_{cus} + OH_{br}$	0.00 (0.08)	−0.09 (−0.09)	1.10×10^{13}	1.73×10^{14}	4.06×10^{12}	6.37×10^{13}
Others							
R36	$O_{2\text{-}cus} \rightarrow O_{cus} + O_{cus}$	0.26 (0.25)	−0.41 (−0.43)	3.41×10^{12}	2.47×10^{12}	4.05×10^{-3}	1.03×10^{10}
R37	$O_{cus} + O_{cus} \rightarrow O_{2\text{-}cus}$	0.67 (0.68)	0.41 (0.43)	3.45×10^{12}	5.51×10^{12}	1.77×10^{-55}	2.12×10^{3}
R38	$OH_{cus} + O_{br} \rightarrow O_{cus} + OH_{br}$	0.29 (0.40)	0.15 (0.15)	4.47×10^{12}	6.84×10^{12}	6.66×10^{-5}	1.58×10^{10}
R39	$O_{cus} + OH_{br} \rightarrow OH_{cus} + O_{br}$	0.14 (0.25)	−0.15 (−0.15)	3.78×10^{12}	4.48×10^{12}	1.39×10^{4}	1.39×10^{11}
R40	$N_{cus} + Ru_{cus} \rightarrow Ru_{cus} + N_{cus}$	1.43 (1.48)	0.00 (0.00)	4.32×10^{12}	1.15×10^{13}	1.21×10^{-68}	7.31×10^{1}
R41	$O_{cus} + Ru_{cus} \rightarrow Ru_{cus} + O_{cus}$	1.20 (1.22)	0.00 (0.00)	3.45×10^{12}	5.51×10^{12}	1.77×10^{-55}	2.12×10^{3}

[a]The values in parentheses are the energies before ZPE correction, and the kinetic parameters are estimated under $P_T = 2 \times 10^{-10}$ Pa. [b]The ΔE of the adsorption and desorption processes are the corresponding E_{ads} and E_{des}.

3. RESULTS

Elementary Reactions. Table 1 summarizes the 41 elementary reaction steps applied in this microkinetic simulation. For ammonia oxidation on the $RuO_2(110)$ surface, the elementary reactions include adsorption−desorption processes of the reactants and products, NH_x (x = 1−3) dehydrogenations, oxidation product formations, and other reactions. In addition, Table 1 also lists the reaction barriers ($E^{\ddagger}$), reaction energies (ΔE), pre-exponential factors (ν), and rate constants (k) of each reaction step at 90 and 670 K. The rate equations of the 41 reactions are listed in the Supporting Information. Most of the elementary steps here have been investigated recently, and the energetics in this study are consistent with previous DFT calculated results.[13−15]

Reactions R1−R9 are the adsorption and desorption processes of the reactants and products in the ammonia oxidation. R1 and R3 are the adsorptions of oxidation reactants (NH_3 and O_2), and the others are the desorption processes of reactants and products (N_2, NO, N_2O, and H_2O). In this work, the adsorptions of oxidation products are ignored; we assume

dx.doi.org/10.1021/cs401070n | ACS Catal. 2014, 4, 639−648

that the desorbed molecules will be taken away from the reacting system immediately. In adsorption processes, the sticking coefficient (S_c) can be expressed by $S_c^0(T)\,f(\theta)$, a value on a clean surface multiplied by a function of surface coverage.[26] For the adsorption of NH_3 molecules, we assumed that the $S_c^0(T)$ is equal 1 and $f(\theta)$ is equal to the fraction of free reaction sites $\theta_{Ru_{cus}}$; for O_2 molecules, the $S_c^0(T)$ was also assumed to be 1, but an additional function was introduced to describe the $f(\theta)$. For the NH_3 molecules, each molecule needs a single Ru_{cus} site for adsorption, so a sticking coefficient directly proportional to the free Ru_{cus} sites is assumed. For the adsorption of O_2 molecules, it requires two adjacent Ru_{cus} sites to form a side-on $O_{2\text{-}cus}$ molecule on the surface, and a further dissociation reaction of $O_{2\text{-}cus}$ (reaction R36) generates O_{cus} atoms on the surface. When the surface coverage reaches a critical value, the two neighbored Ru_{cus} sites will no longer exist on the surface, and the adsorption of O_2 molecules will be inhibited. Recent experimental studies showed that the maximum O_{cus} atom coverage on the $RuO_2(110)$ surface is 75%.[27] In our microkinetic model, we introduce a sigmoidal function that defines the probability of finding the two neighboring empty Ru_{cus} sites to simulate a limited O_{cus} coverage on the $RuO_2(110)$ surface. Figure 1 plots the

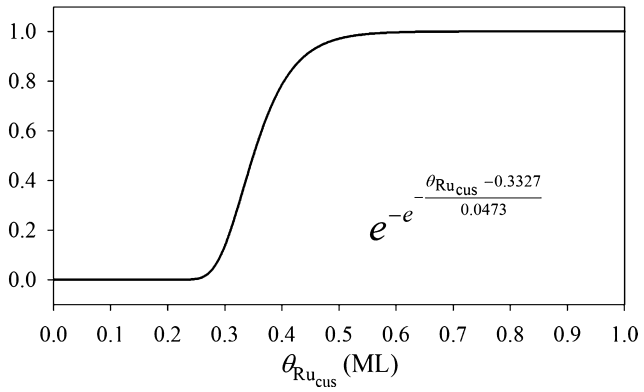

Figure 1. The plot of the Gompertz function applied to correct the sticking coefficient of O_2 on the $RuO_2(110)$ surface.

Gompertz function applied to the O_2 adsorption rate equation (eq S3 in the Supporting Information). This function is artificially designed to adjust the sticking coefficient of the O_2 adsorption. By using the adjusted sticking coefficient, the saturated O_{cus} coverage by the simulation was found to be 0.79 ML, which is close to 0.75 ML from the experimental observation.[27]

Reactions R10−R25 are the possible dehydrogenations and their reverse reactions of NH_x (x = 1−3) species on the surface. For the dehydrogenations of $NH_{3\text{-}cus}$ and $NH_{2\text{-}cus}$, all the reactions are endothermic. Moreover, in reactions R10, R12, and R18, the relative energies of the final states are even higher than the corresponding transition states after the ZPE correction. In the rate equations of these three reactions, the reaction energies are applied as the reaction barriers, and the reaction barriers of corresponding reverse reactions are set to 0 eV. For further dehydrogenations, NH_{cus} molecules are relatively unstable on the $RuO_2(110)$ surface; only the NH_{cus} dehydrogenation to OH_{br} (reaction R23) is endothermic, and the others are exothermic. In addition, the initial states of reactions R22 and R25 are unstable and could not be characterized; the systems spontaneously react to the final state after the structure optimizations. Because of the unstable initial states, the reverse reactions of these two steps are not considered here.

The products of ammonia oxidation on the $RuO_2(110)$ surface are N_2, NO, N_2O, and H_2O; reactions R26−R35 summarize the formation and dissociation of the oxidation products. The calculated barriers and reaction energies are consistent with recent DFT studies.[13−15] Reactions R36 and R37 are the dissociation of the $O_{2\text{-}cus}$ molecule and the recombination of O_{cus} atoms. The calculated $E^{\ddagger}$ and ΔE of reaction R36 are 0.26 and 0.41 eV, respectively; the low energy barrier and exothermic reaction energy indicate that the O_{cus} is the most favored oxygen species on the $RuO_2(110)$ surface. The last four reactions, R38−R41, are the diffusion reactions. R38 and R39 are the H atom diffusion between O_{cus} and O_{br} atoms; R40 and R41 are the diffusions of N_{cus} and O_{cus} atoms on the surface. Reactions R40 and R41 will not alter the equilibrium of the system during the microkinetic simulations because these two reactions will not result in the coverage change of any species (the reactant and the product are the same). However, these two reactions are required for the formations of N-contained oxidation products, and the diffusion barriers (1.43 and 1.20 eV) are relatively greater than the formation barriers of the oxidation products (N_2, NO, and N_2O), which ranged from 0.38 to 0.93 eV.

Because the relatively small formation barrier and desorption energy of $N_{2\text{-}cus}$ are not consistent with the high desorption temperature in experiments,[12] we suggest that the determined step of N_2 production from the $RuO_2(110)$ surface should be the N_{cus} atom diffusion.[13] In KMC simulations by Hong et al., the authors also suggested that the diffusion of N_{cus} should be the rate-limiting process in the formation of N_2 and NO.[14] To obtain a more realistic reacting model, it will be necessary to consider the N_{cus} and O_{cus} diffusions in the microkinetic model. However, because the microkinetic modeling is a mean-field theory, the diffusion steps, such as reactions R40 and R41, will not result in any physical change to a reacting system. Therefore, to consider the diffusion effects in this work, the rate constant of N_{cus} (or O_{cus}) diffusion is applied to the product-formation steps. We applied the rate constant of the N_{cus} diffusion to the rate equations of $N_{2\text{-}cus}$ and N_2O_{cus} formations (Supporting Information eqs S26 and S30). For NO formation, the rate constant of O_{cus} diffusion is considered in the rate equation (Supporting Information eq S28) because the O_{cus} diffusion is faster than the N_{cus} diffusion. Furthermore, the rate constant of O_{cus} recombination reaction (Supporting Information eq S37) is also replaced by that of the O_{cus} diffusion process because the barrier of O_2 recombination ($E^{\ddagger}$ = 0.67 eV) is smaller than that of O_{cus} diffusion ($E^{\ddagger}$ = 1.20 eV).

Batch Type Oxidation. In the adsorption stage of batch type oxidations, the microkinetic model contains six elementary reactions, R1−R4, R36, and R37, and four surface species, Ru_{cus}(vacancy site), $NH_{3\text{-}cus}$, $O_{2\text{-}cus}$, and O_{cus}. The following are the corresponding ODEs in the adsorption processes.

$$\frac{d\theta_{Ru_{cus}}}{dt} = -r_1 + r_2 - 2r_3 + 2r_4 \quad (3\text{-}1)$$

$$\frac{d\theta_{NH_{3\text{-}cus}}}{dt} = r_1 - r_2 \quad (3\text{-}2)$$

$$\frac{d\theta_{O_{2\text{-}cus}}}{dt} = r_3 - r_4 - r_{36} + r_{37} \quad (3\text{-}3)$$

dx.doi.org/10.1021/cs401070n | ACS Catal. 2014, 4, 639−648

$$\frac{d\theta_{O_{cus}}}{dt} = 2r_{36} - 2r_{37} \quad (3\text{-}4)$$

In the simulations of the adsorption process, we followed the concepts from the experimental investigation[12] and adopted a two-step adsorption process: the clean $RuO_2(110)$ surface was exposed to various amounts of O_2 from 0.1 to 1.0 L and then 0.2 L of NH_3 (1L = 1.33×10^{-4} Pa·s). Figure 2a shows the

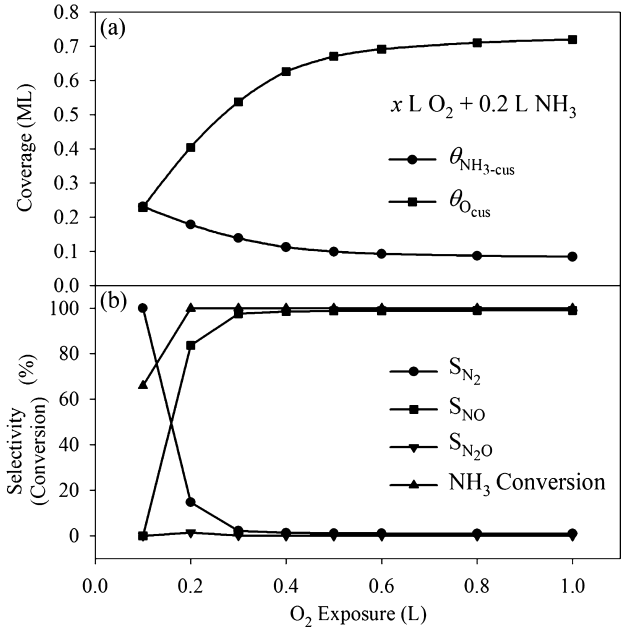

Figure 2. (a) The surface coverage of $NH_{3\text{-cus}}$ and O_{cus} after the adsorption processes and (b) the product selectivities and the NH_3 conversion under various O_2 exposures in batch type ammonia oxidations.

surface compositions after the adsorption process with eight various O_2 exposures (numerical data are listed in the Supporting Information.) Because the rate of $O_{2\text{-cus}}$ decomposition is relatively slow at 90 K, to simplify the simulation, we made an assumption that all the $O_{2\text{-cus}}$ molecules decompose after the adsorption. The coverage of O_{cus} increases as the amount of O_2 exposure is increased, but the limitation from the nature of the O_2 adsorption makes the $\theta_{O_{cus}}$ increase slowly when the exposure is larger than 0.5 L. For the coverage of $NH_{3\text{-cus}}$, it decreases as more O_{cus} atoms adsorbed on the surface because fewer Ru_{cus} sites are available.

After the adsorption processes, the simulations of the batch type ammonia oxidation were performed by following ODEs

$$\frac{d\theta_{Ru_{cus}}}{dt} = r_2 + 2r_4 + r_5 + r_6 + r_7 + r_8 + r_{26} - r_{27} + r_{28} - r_{29} + r_{30} - r_{31} \quad (3\text{-}5)$$

$$\frac{d\theta_{NH_{3\text{-cus}}}}{dt} = -r_2 - r_{10} + r_{11} - r_{12} + r_{13} \quad (3\text{-}6)$$

$$\frac{d\theta_{NH_{2\text{-cus}}}}{dt} = r_{10} - r_{11} + r_{12} - r_{13} - r_{14} + r_{15} - r_{16} + r_{17} - r_{18} + r_{19} \quad (3\text{-}7)$$

$$\frac{d\theta_{NH_{cus}}}{dt} = r_{14} - r_{15} + r_{16} - r_{17} + r_{18} - r_{19} - r_{20} + r_{21} - r_{22} - r_{23} + r_{24} - r_{25} \quad (3\text{-}8)$$

$$\frac{d\theta_{N_{cus}}}{dt} = r_{20} - r_{21} + r_{22} + r_{23} - r_{24} + r_{25} - 2r_{26} + 2r_{27} - r_{28} + r_{29} - r_{30} + r_{31} \quad (3\text{-}9)$$

$$\frac{d\theta_{N_{2\text{-cus}}}}{dt} = -r_5 + r_{26} - r_{27} \quad (3\text{-}10)$$

$$\frac{d\theta_{NO_{cus}}}{dt} = -r_6 + r_{28} - r_{29} - r_{30} + r_{31} \quad (3\text{-}11)$$

$$\frac{d\theta_{N_2O_{cus}}}{dt} = -r_7 + r_{30} - r_{31} \quad (3\text{-}12)$$

$$\frac{d\theta_{O_{2\text{-cus}}}}{dt} = -r_4 - r_{36} + r_{37} \quad (3\text{-}13)$$

$$\frac{d\theta_{O_{cus}}}{dt} = -r_{12} + r_{13} - r_{16} + r_{17} - r_{22} - r_{28} + r_{29} + r_{32} - r_{33} + 2r_{36} - 2r_{37} + r_{38} - r_{39} \quad (3\text{-}14)$$

$$\frac{d\theta_{O_{br}}}{dt} = -r_{10} + r_{11} - r_{14} + r_{15} - r_{20} + r_{21} + r_{34} - r_{35} - r_{38} + r_{39} \quad (3\text{-}15)$$

$$\frac{d\theta_{OH_{cus}}}{dt} = r_{12} - r_{13} + r_{16} - r_{17} - r_{18} + r_{19} + r_{22} - r_{25} - 2r_{32} + 2r_{33} - r_{34} + r_{35} - r_{38} + r_{39} \quad (3\text{-}16)$$

$$\frac{d\theta_{OH_{br}}}{dt} = r_{10} - r_{11} + r_{14} - r_{15} + r_{20} - r_{21} - r_{23} + r_{24} - r_{34} + r_{35} + r_{38} - r_{39} \quad (3\text{-}17)$$

$$\frac{d\theta_{H_2O_{cus}}}{dt} = -r_8 + r_{18} - r_{19} + r_{25} + r_{32} - r_{33} + r_{34} - r_{35} \quad (3\text{-}18)$$

$$\frac{d\theta_{H_2O_{br}}}{dt} = -r_9 + r_{23} - r_{34} \quad (3\text{-}19)$$

The eight sets of surface compositions from different O_2 exposures were applied as the initial coverages in the simulations of the oxidation processes. In this step, all the elementary reactions are involved in the microkinetic model except the adsorption steps (R1 and R3). In the batch oxidations, the simulation temperature ranged from 90 to 640 K with a 1 K/s heating rate; the system pressure was kept at 10^{-10} Pa, where all the adsorptions are ignored. Figure 2b shows the selectivities (S) to the nitrogen-containing (N-containing) products and the NH_3 conversion (numerical data are listed in the Supporting Information), and Figure 3 shows the TPD spectra of all the oxidation products. For ammonia oxidation, the $\theta_{Ocus}/\theta_{NH_{3-cus}}$ ratio has to be >1.5 to complete the dehydrogenations and >2.5 to achieve total oxidation. The simulations showed that the $\theta_{Ocus}/\theta_{NH_{3-cus}}$ ratio exceeds 2.5 when the O_2 exposure is more than 0.3 L and NO becomes the

dx.doi.org/10.1021/cs401070n | ACS Catal. 2014, 4, 639−648

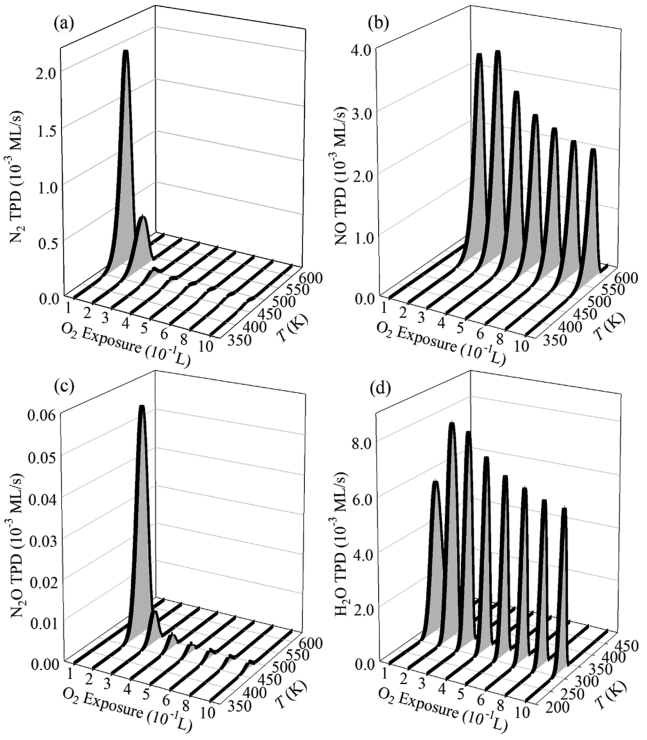

Figure 3. The simulated TPD spectra of (a) N_2, (b) NO, (c) N_2O, and (d) H_2O in batch type oxidations with different amounts of O_2 exposure.

dominant oxidation product in the oxidation. Figure 3a shows that almost no N_2 could be produced with the high O_2 exposures. When the O_2 exposure is 0.1 L, the coverage of O_{cus} is too low to complete the dehydrogenations, so the $NH_{3\text{-cus}}$ cannot be 100% converted, and hence, NO cannot be produced in the oxidation.

At intermediate O_{cus} coverage, the O_2 exposure is 0.2 L, and $\theta_{O_{cus}}/\theta_{NH_{3\text{-cus}}}$ lies between 1.5 and 2.5; all the $NH_{3\text{-cus}}$ is completely dehydrogenated (the NH_3 conversion is 100%) but not totally oxidized. The simulated results show that N_2O is not a favored product in batch type ammonia oxidation. The highest N_2O desorption rate appears when the O_2 exposure is 0.2 L (Figure 3c); however, the amplitude of its desorption peak is relatively low, and the corresponding selectivity (S_{N_2O}) is 1.48%. In simulations of batch type ammonia oxidations, elementary reactions related to O_{br} or OH_{br} species were considered in the microkinetic model to check their contributions to reactions on the surface. During the oxidation processes, OH_{br} is one of the intermediates on the surface, but there is no H_2O_{br} desorbed in the whole temperature range. This result indicates that O_{br} atoms are involved in dehydrogenations, but it is not an oxidant in the overall ammonia oxidation reactions.

Steady-State Oxidation. In the simulations of the steady-state oxidation, the partial pressure of NH_3 was fixed at 1×10^{-5} Pa. We examined the system in eight O_2 and NH_3 pressure ratios (P_{O_2}/P_{NH_3}), and the calculated values are 0.5, 1, 2, 4, 6, 10, 15, and 20. For each ratio, the simulating temperature is from 480 to 670 K with a step size of 10 K. To simplify the simulations, the reactions related to bridge site species (O_{br}, OH_{br} and H_2O_{br}) were not considered in the microkinetic model of the steady-state oxidation. That is because the simulations in the previous section show that the O_{br} is not the oxidant in the overall ammonia oxidation reaction. The following are the ODEs applied in the steady-state oxidation simulations:

$$\frac{d\theta_{Ru_{cus}}}{dt} = -r_1 + r_2 - 2r_3 + 2r_4 + r_5 + r_6 + r_7 + r_8 + r_{26} - r_{27} + r_{28} - r_{29} + r_{30} - r_{31} \quad (3\text{-}20)$$

$$\frac{d\theta_{NH_{3\text{-cus}}}}{dt} = r_1 - r_2 - r_{12} + r_{13} \quad (3\text{-}21)$$

$$\frac{d\theta_{NH_{2\text{-cus}}}}{dt} = r_{12} - r_{13} - r_{16} + r_{17} - r_{18} + r_{19} \quad (3\text{-}22)$$

$$\frac{d\theta_{NH_{cus}}}{dt} = r_{16} - r_{17} + r_{18} - r_{19} - r_{22} - r_{25} \quad (3\text{-}23)$$

$$\frac{d\theta_{N_{cus}}}{dt} = r_{22} + r_{25} - 2r_{26} + 2r_{27} - r_{28} + r_{29} - r_{30} + r_{31} \quad (3\text{-}24)$$

$$\frac{d\theta_{N_{2\text{-cus}}}}{dt} = -r_5 + r_{26} - r_{27} \quad (3\text{-}25)$$

$$\frac{d\theta_{NO_{cus}}}{dt} = -r_6 + r_{28} - r_{29} - r_{30} + r_{31} \quad (3\text{-}26)$$

$$\frac{d\theta_{N_2O_{cus}}}{dt} = -r_7 + r_{30} - r_{31} \quad (3\text{-}27)$$

$$\frac{d\theta_{O_{2\text{-cus}}}}{dt} = r_3 - r_4 - r_{36} + r_{37} \quad (3\text{-}28)$$

$$\frac{d\theta_{O_{cus}}}{dt} = -r_{12} + r_{13} - r_{16} + r_{17} - r_{22} - r_{28} + r_{29} + r_{32} - r_{33} + 2r_{36} - 2r_{37} \quad (3\text{-}29)$$

$$\frac{d\theta_{OH_{cus}}}{dt} = r_{12} - r_{13} + r_{16} - r_{17} - r_{18} + r_{19} + r_{22} - r_{25} - 2r_{32} + 2r_{33} \quad (3\text{-}30)$$

$$\frac{d\theta_{H_2O_{cus}}}{dt} = -r_8 + r_{18} - r_{19} + r_{25} + r_{32} - r_{33} \quad (3\text{-}31)$$

Figure 4 summarizes the simulated NH_3 conversion (a) and selectivities to N-containing oxidation products (b–d). The numerical data of the NH_3 conversion, selectivities, and TOFs of products are summarized in the Supporting Information. Similar to the batch type ammonia oxidation, the partial pressure of O_2 directly affects the selectivities to N_2 (S_{N_2}) and NO (S_{NO}). When the P_{O_2}/P_{NH_3} ratio is 0.5 and 1, the amount of O_{cus} is insufficient to make NH_3 molecules totally oxidized; even all the adsorbed O_2 molecules are dissociated. Therefore, N_2 is the major oxidation product under these conditions. In the steady-state ammonia oxidations, the system temperature also affects the selectivities. The N_2 selectivity approaches 100% in all the P_{O_2}/P_{NH_3} ratios at 480–500 K: when the P_{O_2}/P_{NH_3} is >2, the S_{N_2} decreases dramatically from 510 to 570 K and increases again when the temperature is higher than 600 K. The selectivity to NO in Figure 4c is roughly an inverse of Figure

dx.doi.org/10.1021/cs401070n | ACS Catal. 2014, 4, 639–648

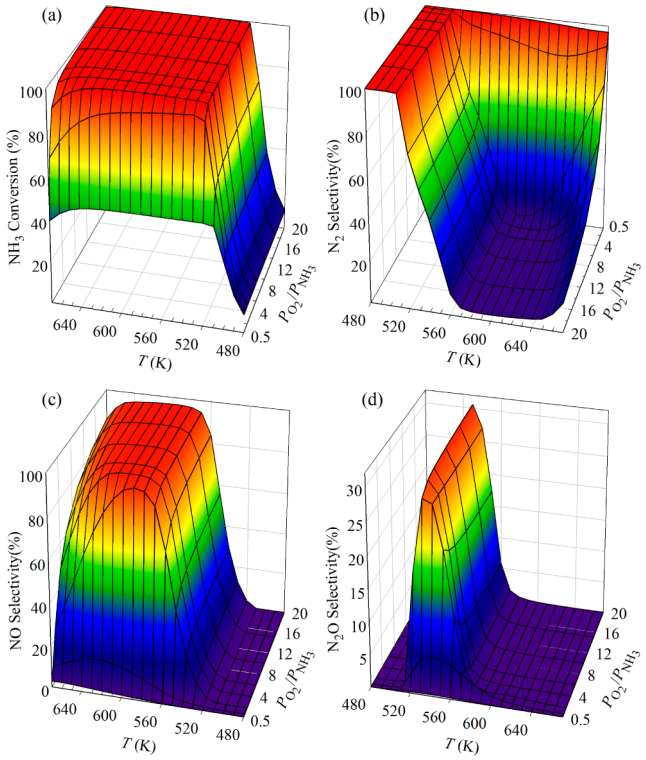

Figure 4. (a) NH_3 conversion and (b–d) selectivities to N-containing products in steady-state ammonia oxidations as functions of temperature and P_{O_2}/P_{NH_3}.

4b, which means the N_2 and NO are the major products of the ammonia oxidation on the $RuO_2(110)$ surface. In addition, the large highland area in Figure 4c shows that NO is a more preferred product. Different from the batch type oxidation, N_2O is one of the products in steady-state oxidation. The temperature of the N_2O production lies between 510 and 570 K; the highest N_2O selectivity is around 35% and appears at 520 K. The mechanisms of the oxidation reactions will be discussed in the next section.

4. DISCUSSION

The microkinetic models in this study are based on the same elementary steps, but the simulated results showed that the reaction mechanisms of these two ammonia oxidation methods are quite different. Since the initial coverage of reactants directly alters the final selectivity to products, when compared with the steady-state oxidation, the mechanism of the batch type ammonia oxidation is relatively simple. To understand the oxidation mechanism, the coverage of N-containing surface species during the batch type oxidation (O_2 exposure = 0.2 L) is plotted in Figure 5. This figure clearly shows that the decomposition of NH_3 starts at 250 K, and all the dehydrogenations finish at 350 K. As the temperature increases, NO_{cus} starts to be formed on the surface at 400 K and completely desorbs from the surface at 600 K. In this work, the formations of $N_{2\text{-cus}}$ and N_2O_{cus} are governed by the N_{cus} diffusion. This diffusion barrier is higher than the desorption energies of $N_{2\text{-cus}}$ and N_2O_{cus}, which implies that $N_{2\text{-cus}}$ and N_2O_{cus} will desorb immediately after they are formed on the $RuO_2(110)$ surface. Therefore, in these three N-containing products, only NO_{cus} molecules could be detected on the $RuO_2(110)$ surface. This result is consistent with the

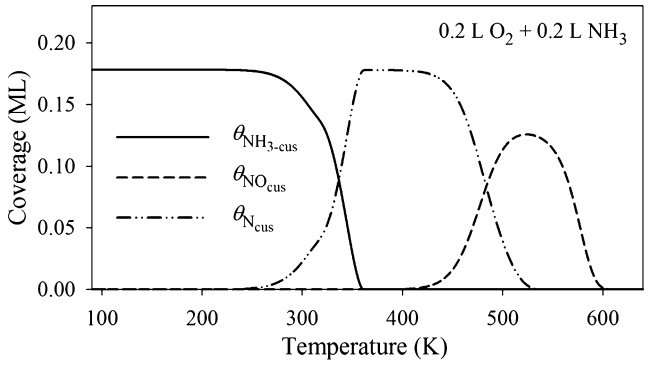

Figure 5. The surface coverage of $NH_{3\text{-cus}}$, NO_{cus}, and N_{cus} during the batch type ammonia oxidation with 0.2 L of O_2 exposure.

experimental observation that no N–N stretching mode was detected in high-resolution electron energy-loss spectroscopy during batch type ammonia oxidation.[12] Similarly, $N_{2\text{-cus}}$ and N_2O_{cus} cannot be observed on the $RuO_2(110)$ surface during steady-state ammonia oxidation. Figure 6 shows the surface

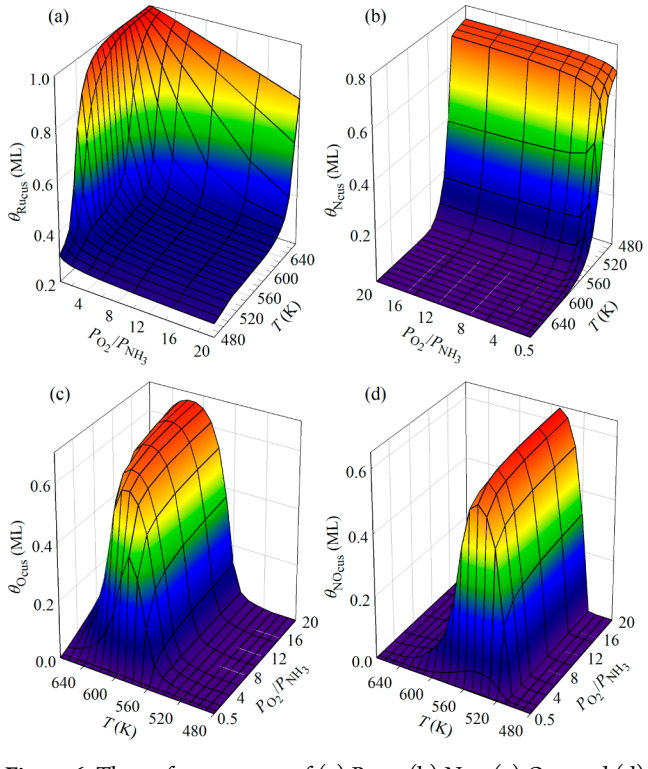

Figure 6. The surface coverage of (a) Ru_{cus}, (b) N_{cus}, (c) O_{cus}, and (d) NO_{cus} in steady-state ammonia oxidations as functions of temperature and P_{O_2}/P_{NH_3}.

coverage of Ru_{cus}, N_{cus}, O_{cus}, and NO_{cus} in the steady-state oxidation (numerical data are summarized in the Supporting Information); the summation of coverage of these four species is very close to 1 ML.

In both ammonia oxidation methods, the abundance of O_2 results in a high selectivity to NO, but this effect becomes insignificant when the amount of O_{cus} exceeds the critical value. In batch oxidation, the selectivities are almost the same when the O_2 exposure is >0.3 L; in steady-state oxidation, the shape of selectivity curves are very similar when $P_{O_2}/P_{NH_3} \geq 2$. As mentioned in the previous section, the stoichiometric $\theta_{O_{cus}}/$

dx.doi.org/10.1021/cs401070n | ACS Catal. 2014, 4, 639–648

$\theta_{NH_{3-cus}}$ ratio to complete the NH_3 dehydrogenation is 1.5. Therefore, in batch type oxidation, the insufficiency of the O_{cus} atom makes the NO selectivity closer to 0% when $\theta_{O_{cus}}/\theta_{NH_{3-cus}} \leq 1.5$. In steady-state oxidation, N_2 is the major oxidation product when the P_{O_2}/P_{NH_3} ratio is small, but it never reaches 100% selectivity. Figure 4c shows that NO can be still produced in the oxidation when the P_{O_2}/P_{NH_3} is 0.5 (the lowest feeding ratio in this work). In the batch type oxidation, a gradually increased temperature makes the dehydrogenation, product formation, and desorption proceed step by step. In contrast, in steady-state oxidation, the reactants are continuously supplied, and most of the reactions can occur at the same time under a fixed temperature.

In steady-state oxidations, N_2 is the dominant product in the entire temperature range when the P_{O_2}/P_{NH_3} is 0.5 and 1. The relatively low O_2 partial pressure directly suppresses the NO formation, and the change in the temperature does not alter the oxidation significantly. However, as the $P_{O_2}/P_{NH_3} \geq 2$, the system temperature is the main controlling factor of the oxidation reaction. In the low temperature region (T = 480−500 K), N_2 is the major oxidation product with a selectivity higher than 97%, and Figure 6 shows that N_{cus} is the major species (~0.7 ML) on the surface. Although a high S_{N_2} could be obtained, the NH_3 conversion is relatively low under this temperature range. At 480−500 K, the O_2 adsorption rates range from 0.001 to 0.005 ML/s, where the rates of NH_3 adsorptions are 0.015−0.021 ML/s (the adsorption rates are listed in the Supporting Information). Obviously, the O_2 adsorption rates are much slower than those of NH_3 adsorptions, which explains the low NO selectivity under these temperatures. As the system temperature becomes higher than 500 K, the O_2 adsorption rate will be fast enough to generate NO_{cus} molecules by the excess O_{cus} atoms on the surface. As shown in Figure 6c, the O_{cus} coverage increases dramatically from 520 to 600 K, where the NO selectivity also increases in this temperature region and reaches the maximum at 600 K. The increasing temperature results in an increase in the O_2 adsorption and the $O_{2\text{-}cus}$ dissociation rates; however, it also improves the rates of the O_{cus} recombination and the $O_{2\text{-}cus}$ desorption. For example, at P_{O_2}/P_{NH_3} = 2, the O_2 adsorption rate increased 0.0259 ML/s from 600 K (0.0445 ML/s) to 670 K (0.0704 ML/s), where the desorption rate increased 0.0274 ML/s (from 0.0081 to 0.0355 ML/s). As the system temperature increases above 600 K, the increasing $O_{2\text{-}cus}$ desorption rate becomes significant, and the coverage of O_{cus} on the $RuO_2(110)$ surface starts to decrease; furthermore, it reflects the decreasing of NO selectivity.

The production of N_2O is another difference between the two ammonia oxidation methods. On the $RuO_2(110)$ surface, N_2O is produced via the recombination of N_{cus} and NO_{cus}; it is a secondary product in ammonia oxidation because the production of N_2O occurs after NO_{cus} appears on the surface. Therefore, the existence of NO_{cus} on the surface is a basic requirement for N_2O_{cus} production. In addition, the barrier of N_{cus} + O_{cus} recombination is smaller than that of N_{cus} + NO_{cus} recombination; the existence of O_{cus} on the surface will reduce the probability of N_2O_{cus} formation. For the reasons above, it is easy to understand why N_2O is not a favorable product in batch type oxidation.

The highest selectivity to N_2O in batch type oxidation is 1.48%, but it reaches 30.59% in steady-state oxidations. As shown in Figure 4d, when the temperature lies between 500 and 570 K, N_2O is one of favored oxidation products ($P_{O_2}/P_{NH_3} \geq 2$). The production of N_2O is located at an intermediate region where the growth of $\theta_{NO_{cus}}$ and the decay of $\theta_{N_{cus}}$ crosses (Figures 6b and 6d); this intermediate region also lies between the high S_{N_2} and S_{NO}. In this temperature range, both N_{cus} and NO_{cus} exist constantly on the $RuO_2(110)$ surface, which makes the N_2O_{cus} formation a possible reaction. When the system temperature is lower than 500 K, there is no sufficient NO_{cus} for N_2O_{cus} formation; on the other hand, when the temperature is higher than 570 K, NO_{cus} molecules could effectively desorb from the surface which reduces the probability of N_{cus} + NO_{cus} recombination. The production of N_2O is very favorable when using steady-state oxidation, but the S_{N_2O} remains at about 30% when the P_{O_2}/P_{NH_3} ratio increases from 2 to 20. Because of the nature of the formation mechanism, N_2O still cannot be a major oxidation product on the $RuO_2(110)$ surface.

The simulated results demonstrated that the surface composition determines the selectivities in the steady-state oxidation, and the adsorption rates of reactants directly affect the coverage of the surface species. In addition to the temperature and the P_{O_2}/P_{NH_3} ratio, the total pressure of the system is another factor that alters the adsorption rates. To investigate the pressure effect, we examined the NH_3 partial pressure, varied from 10^{-6} to 10^{3} Pa in the steady-state oxidations. In this series of simulations, the P_{O_2}/P_{NH_3} ratio was fixed at 2, and the simulating temperature was 670 K. We chose P_{O_2}/P_{NH_3} = 2 because it is the intermediate ratio between the high S_{N_2} and S_{NO}, and the high temperature could minimize the difference of the reaction rate between the elementary steps. Figure 7a plots the selectivities to the N-containing products,

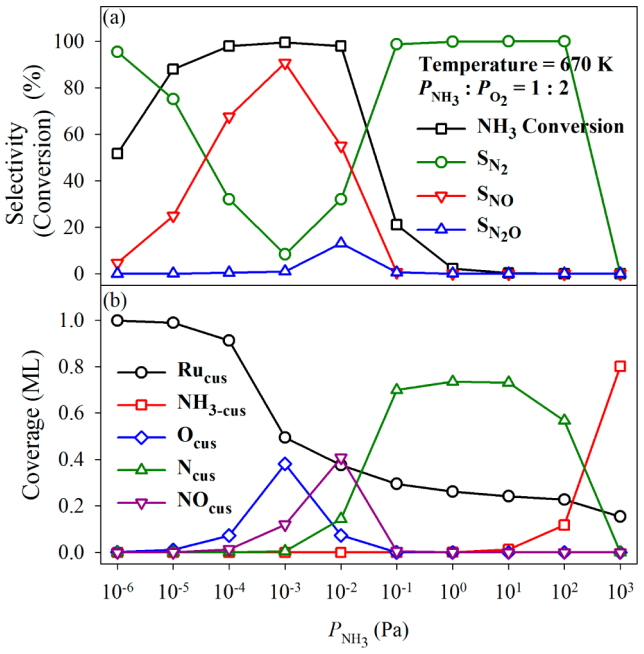

Figure 7. (a) NH_3 conversion and selectivities and (b) the surface composition in steady-state oxidations with different NH_3 partial pressures. The simulating temperature is 670 K, and P_{O_2}/P_{NH_3} = 2.

dx.doi.org/10.1021/cs401070n | ACS Catal. 2014, 4, 639−648

and the conversion of NH_3 and Figure 7b shows the coverage of surface species at steady state (numerical data are listed in Supporting Information). At $P_{NH_3} = 10^{-3}$ Pa, the system reaches the highest $\theta_{O_{cus}}$, and the NO selectivity reaches the maximum value (90.72%). In addition, the highest S_{N_2O} (13.01%) appears at $P_{NH_3} = 10^{-2}$ Pa, where the system has the highest $\theta_{NO_{cus}}$ under this pressure. When $P_{NH_3} \geq 10^{-1}$ Pa, N_2 is the dominant product in the oxidation. In the examination of pressure effects, the NH_3 adsorption rate increases as the P_{NH_3} increases, but the O_2 adsorption rate reaches the maximum value at $P_{NH_3} = 10^{-1}$ Pa ($P_{O_2} = 2 \times 10^{-1}$ Pa) and decreases when $P_{O_2} \geq 2 \times 10^{-1}$ Pa (the values of adsorption/desorption rates are listed in the Supporting Information). When $P_{NH_3} \geq 10^{-1}$, the much faster NH_3 adsorption rate than that of O_2 means most of the Ru_{cus} sites are occupied by N_{cus} atoms, which results in a high selectivity of N_2 ($S_{N_2} > 98\%$). This simulated result is consistent with experimental observations by Pérez-Ramírez et al.,[15] who showed that N_2 is the major oxidation product under the ambient pressure, where the S_{N_2} ranges from 83% to 95%. Again, the high N_2 selectivity is companied by low NH_3 conversion. At $P_{NH_3} = 10^{-1}$ Pa, 70% of surface Ru_{cus} sites are occupied by N_{cus} atoms, and only 21.08% of NH_3 could be converted because of the relatively slow O_2 adsorption rate. Because the NH_3 partial pressure is $>10^1$ Pa, the N_2 selectivity is >99.99%, and the dramatically elevated NH_3 adsorption rate results in unreacted NH_3 molecules' appearance on the $RuO_2(110)$ surface. At $P_{NH_3} = 10^3$ Pa, the NH_3 adsorption rate is extremely fast; 80% of surface sites are occupied by NH_3 molecules. Under this condition, the NH_3 conversion is 0% because of the zero O_2 adsorption.

Summarizing the simulation results in this study, the selectivities of the products in the ammonia oxidations are based on the surface compositions. For example, the high O_{cus} coverage leads to the high NO selectivity. In batch oxidations, the initial coverage of O_{cus} and $NH_{3\text{-}cus}$ can be controlled in the adsorption process. In steady-state oxidations, the surface compositions depend on the adsorption/desorption rates of the reactants; the parameters affect the adsorption/desorption rates, including the formation barrier of the products, system temperature, the ratio in partial pressure, and the total pressure of the oxidation system. The DFT calculated results indicate that $N_{2\text{-}cus}$ has the lowest formation barrier (0.38 eV) among the three N-containing products in ammonia oxidation. However, according the microkinetic simulations, N_2 is not the dominant product under all oxidizing conditions. Ab initio methods provide only independent information of elementary reactions; kinetic simulations are required to connect all the reactions and mimic a real reacting system.

5. CONCLUSION

We established a microkinetic model to simulate ammonia oxidation on the $RuO_2(110)$ surface. The microkinetic simulations successfully demonstrate the differences in reaction mechanisms between batch type and steady-state oxidations of ammonia. The major oxidation products of ammonia oxidation are N_2 and NO. The simulated results showed that more O_{cus} on the surface results in a higher selectivity to NO, and less O_{cus} leads to a higher S_{N_2}, but the small O_{cus} coverage will result in a low NH_3 conversion at the same time. The way to adjust the selectivities is to change the O_{cus} coverage on the surface. In batch type oxidations, controlling the θ_{Ocus} is relatively easy because the $\theta_{O_{cus}}/\theta_{NH_{3-cus}}$ ratio could be easily determined in the adsorption processes. In contrast, steady-state ammonia oxidation is more complicated; the oxidizing temperature, total pressure, and P_{O_2}/P_{NH_3} ratio are the parameters that could alter the selectivities. The following summarize the optimal conditions to obtain high selectivity to each N-containing molecule in steady-state ammonia oxidations:

1. N_2: Proceed with the oxidation under low temperature (480−500 K), small P_{O_2}/P_{NH_3} ratio (≤1), and NH_3 partial pressure $>10^{-1}$ Pa.
2. NO: Keep the oxidizing temperature higher than 570 K, and use a large P_{O_2}/P_{NH_3} ratio and a system total pressure around 10^{-3} Pa.
3. N_2O: Maintain the oxidizing temperature at 500−570 K and the NH_3 partial pressure around 10^{-2} Pa.

N_2O production, is not favored in batch type oxidation, and the highest selectivity in steady-state oxidation is ∼30%. N_2O is a secondary product and could be a only minor product in steady-state oxidation because its formation requires the appearance of NO_{cus} on the surface. This study demonstrates that microkinetic simulations could provide an effective method to predict oxidizing conditions for the products and could be a useful tool to investigate heterogeneous catalytic reactions.

■ ASSOCIATED CONTENT

Supporting Information

The rate equations of the 41 elementary reactions and the numerical data of the conversions, TOFs, selectivities, surface coverages, and adsorption/desorption rates of reactants under each oxidation condition. This material is available free of charge via the Internet at http://pubs.acs.org.

■ AUTHOR INFORMATION

Corresponding Author

*Phone: +886-2-27376653. Fax: +886-2-27376644. E-mail: jcjiang@mail.ntust.edu.tw.

Notes

The authors declare no competing financial interest.

■ ACKNOWLEDGMENTS

We gratefully acknowledge support from the National Science Council of Taiwan (NSC 101-2113-M-011-004-MY3) and the computer time and facilities from National Center for High-Performance Computing (NCHC).

■ REFERENCES

(1) Gokhale, A. A.; Kandoi, S.; Greeley, J. P.; Mavrikakis, M.; Dumesic, J. A. *Chem. Eng. Sci.* **2004**, *59*, 4679−4691.
(2) Gokhale, A. A.; Dumesic, J. A.; Mavrikakis, M. *J. Am. Chem. Soc.* **2008**, *130*, 1402−1414.
(3) Grabow, L. C.; Gokhale, A. A.; Evans, S. T.; Dumesic, J. A.; Mavrikakis, M. *J. Phys. Chem. C* **2008**, *112*, 4608−4617.
(4) Madon, R. J.; Braden, D.; Kandoi, S.; Nagel, P.; Mavrikakis, M.; Dumesic, J. A. *J. Catal.* **2011**, *281*, 1−11.
(5) Novell-Leruth, G.; Ricart, J. M.; Perez-Ramirez, J. *J. Phys. Chem. C* **2008**, *112*, 13554−13562.
(6) Kandoi, S.; Greeley, J.; Sanchez-Castillo, M. A.; Evans, S. T.; Gokhale, A. A.; Dumesic, J. A.; Mavrikakis, M. *Top. Catal.* **2006**, *37*, 17−28.

(7) Bjorkman, K. R.; Schoenfeldt, N. J.; Notestein, J. M.; Broadbelt, L. J. *J. Catal.* **2012**, *291*, 17−25.
(8) Blaylock, D. W.; Ogura, T.; Green, W. H.; Beran, G. J. O. *J. Phys. Chem. C* **2009**, *113*, 4898−4908.
(9) Cao, X.-M.; Burch, R.; Hardacre, C.; Hu, P. *Catal. Today* **2011**, *165*, 71−79.
(10) Sutton, J. E.; Panagiotopoulou, P.; Verykios, X. E.; Vlachos, D. G. *J. Phys. Chem. C* **2013**, *117*, 4691−4706.
(11) Wang, C.-C.; Wu, J.-Y.; Jiang, J.-C. *J. Phys. Chem. C* **2013**, *117*, 6136−6142.
(12) Wang, Y.; Jacobi, K.; Schöne, W. D.; Ertl, G. *J. Phys. Chem. B* **2005**, *109*, 7883−7893.
(13) Wang, C.-C.; Yang, Y.-J.; Jiang, J.-C.; Tsai, D.-S.; Hsieh, H.-M. *J. Phys. Chem. C* **2009**, *113*, 17411−17417.
(14) Hong, S.; Karim, A.; Rahman, T. S.; Jacobi, K.; Ertl, G. *J. Catal.* **2010**, *276*, 371−381.
(15) Perez-Ramirez, J.; Lopez, N.; Kondratenko, E. V. *J. Phys. Chem. C* **2010**, *114*, 16660−16668.
(16) Cui, X.; Zhou, J.; Ye, Z.; Chen, H.; Li, L.; Ruan, M.; Shi, J. *J. Catal.* **2010**, *270*, 310−317.
(17) Zweidinger, S.; Hofmann, J. P.; Balmes, O.; Lundgren, E.; Over, H. *J. Catal.* **2010**, *272*, 169−175.
(18) Hevia, M. A. G.; Amrute, A. P.; Schmidt, T.; Pérez-Ramírez, J. *J. Catal.* **2010**, *276*, 141−151.
(19) Over, H.; Kim, Y. D.; Seitsonen, A. P.; Wendt, S.; Lundgren, E.; Schmid, M.; Varga, P.; Morgante, A.; Ertl, G. *Science* **2000**, *287*, 1474−1476.
(20) Liu, Z.-P.; Hu, P.; Alavi, A. *J. Chem. Phys.* **2001**, *114*, 5956−5957.
(21) Kresse, G.; Hafner, J. *Phys. Rev. B* **1993**, *48*, 13115−13118.
(22) Kresse, G.; Furthmuller, J. *Phy. Rev. B* **1996**, *54*, 11169−11186.
(23) Kresse, G.; Furthmüller, J. *Comput. Mater. Sci.* **1996**, *6*, 15−50.
(24) Perdew, J. P. In *Electronic Structure of Solids '91*; Zieche, P., Eschrig, H., Eds.; Akademie Verlag: Berlin, 1991; p 11.
(25) Kresse, G.; Joubert, D. *Phys. Rev. B* **1999**, *59*, 1758−1775.
(26) Cortright, R. D.; Dumesic, J. A. *Adv. Catal.* **2001**, *46*, 161−264.
(27) Kim, Y. D.; Seitsonen, A. P.; Wendt, S.; Wang, J.; Fan, C.; Jacobi, K.; Over, H.; Ertl, G. *J. Phys. Chem. B* **2001**, *105*, 3752−3758.